ELSEVIER

Journal of Materials Processing Technology 194 (2007) 52–62

Journal of Materials Processing Technology

www.elsevier.com/locate/jmatprotec

The effect of anisotropy on the deformation and fracture of sapphire wafers subjected to thermal shocks

T. Vodenitcharova [a], L.C. Zhang [a,*], I. Zarudi [a], Y. Yin [b], H. Domyo [c], T. Ho [c], M. Sato [c]

[a] *School of Aerospace, Mechanical and Mechatronic Engineering, The University of Sydney, 2006 NSW, Australia*
[b] *School of Physics, The University of Sydney, 2006 NSW, Australia*
[c] *Peregrine Semiconductor Australia Pty Ltd., 8 Herb Elliott Avenue, Homebush Bay, NSW 2127, Australia*

Received 15 January 2007; received in revised form 27 February 2007; accepted 28 March 2007

Abstract

This paper studies the effect of anisotropy on the response of an *R*-plane sapphire wafer to a rapid thermal loading. The finite element method was used to analyse the temperature and stress distribution in the wafer when the environment was heated from room temperature to 800 °C, and then cooled down to room temperature. To determine the weak and strong points along the wafer edge, fracture criteria for anisotropic materials were applied. It was found that the maximum tensile stresses occur at the flat wafer edge on cooling down, and could fracture the wafer, most likely at a location of a high tensile stress and in a direction of a weak cleavage plane. The wafer appears to be most prone to fracture at its flat edge, and would crack in the weakest plane $(0\,1\,\bar{1}\,2)$. The strongest points along the edge are located at the sides of the flat edge, where the tensile stresses in the wafer plane are the lowest. A circular wafer subjected to the same thermal loading was also analysed for comparison, and the weakest and strongest locations and cleavage planes were determined.

Keywords: Sapphire wafers; Thermal shock; Thermal stresses; Anisotropy

1. Introduction

Single crystal sapphire (α-alumina, Al_2O_3) offers superior physical, chemical and optical properties, which make it an excellent material for applications, such as high-speed IC chips, thin-film substrates, and various electronic and mechanical components [1–3]. Sapphire substrates are often manufactured with different orientations. For example, substrates in the C-plane $(0\,0\,0\,1)$ are useful for infrared detector applications; substrates in the A-plane $(1\,1\,\bar{2}\,0)$ are applicable to high-speed superconductors; and substrates in the *R*-plane $(1\,\bar{1}\,0\,2)$ are used for hetero-epitaxial deposition of silicon for microelectronic IC applications.

Nevertheless, wafers made of single crystal sapphire are brittle and can fracture under high tensile stresses during fabrication and application. Such stresses can occur, for example, in rapid thermal processing in a horizontal tube. It has been observed that *R*-plane sapphire wafers sometimes break, when withdrawn from the furnace, predominantly normal to the flat wafer edge, Fig. 1.

The aim of the present paper is to study the relative possibility of onset of fracture in an *R*-plane sapphire wafer subjected to thermal loading. The influence of anisotropy will be taken into account to determine the weak and strong points along the wafer circumference. The material properties of the anisotropic sapphire will be investigated first, and then the finite element method will be used to carry out the thermal stress analysis.

2. Properties of single crystal sapphire

2.1. Elastic properties

α-Alumina, Al_2O_3 is a hard, brittle material having a hexagonal-rhombohedral structure, whose physical properties and surface energies depend on the crystallographic orientation. Fig. 2(a) shows a primitive cell of the sapphire crystal, having lattice parameters $a = 4.758$ Å and $c = 12.991$ Å. In the same figure, $a_1a_2a_3c$ denotes the hexagonal coordinate system

* Corresponding author. Tel.: +61 2 9351 2835; fax: +61 2 9351 7060.
E-mail address: Zhang@aeromech.usyd.edu.au (L.C. Zhang).

0924-0136/$ – see front matter © 2007 Elsevier B.V. All rights reserved.
doi:10.1016/j.jmatprotec.2007.03.125

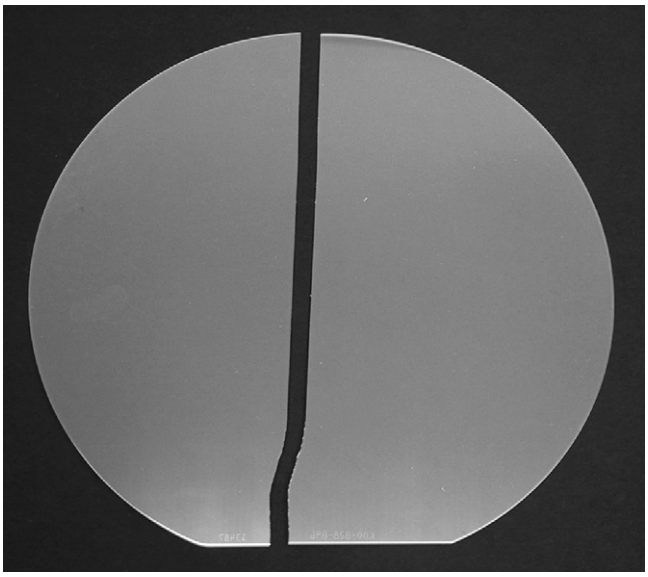

Fig. 1. A cracked wafer after withdrawal from a processing tube.

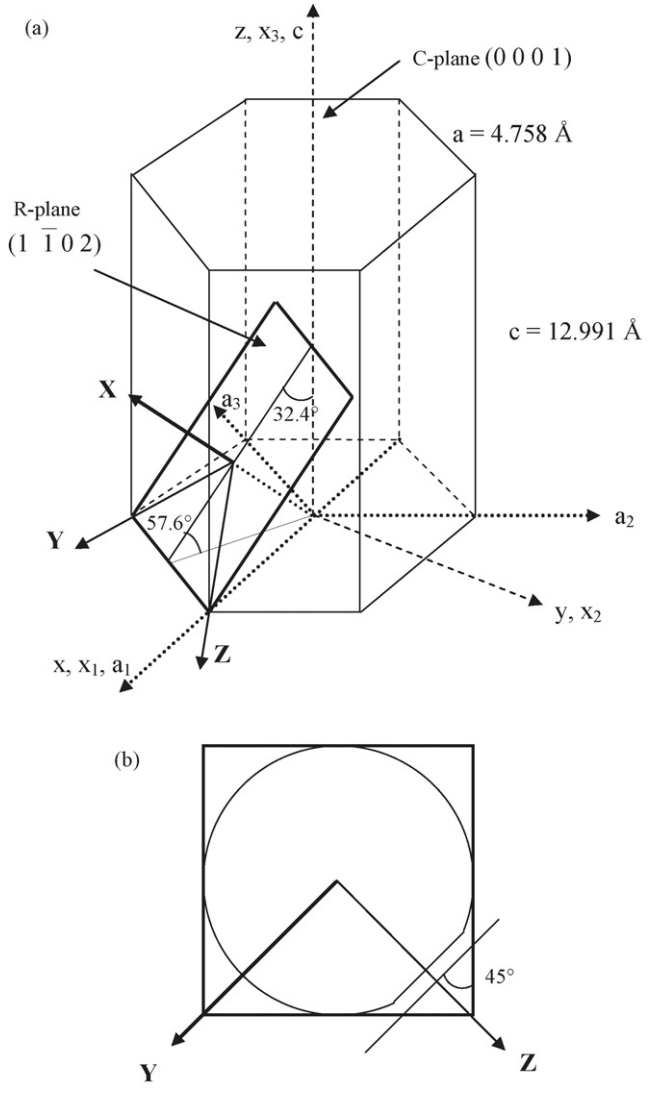

Fig. 2. (a) Coordinate systems in the sapphire crystal, and the *R*-plane and (b) a sapphire wafer in the *R*-plane, and the coordinate system in the FEA simulations.

used for the Miller-Bravais notations of the various crystallographic planes and orientations, $x_1x_2x_3$ indicates the rectangular cartesian coordinate system in which the elastic properties of sapphire are specified, and xyz is the coordinate system which will be used later in the present paper. Fig. 2(b) shows the *R*-plane of the crystal, i.e., a plane inclined at an angle of 32.4° to the *c*-axis, and the *R*-plane sapphire wafer considered in the paper.

The elastic properties of single crystal sapphire are defined by its elastic constants C_{ij}, usually determined in the coordinate system $x_1x_2x_3$ shown in Fig. 2(a). For a generally anisotropic elastic material, the elastic constants link the stress tensor σ to the strain tensor ε through the generalized Hooke's law:

$$\sigma_{mn} = C_{mnpq}\varepsilon_{pq} \tag{1}$$

or

$$\varepsilon_{mn} = S_{mnpq}\sigma_{pq} \tag{2}$$

where C_{mnpq} are the components of the elasticity (stiffness) tensor C ($m, n, p, q = 1, 2, 3$), and S_{mnpq} are the components of the compliance tensor S, so that $S = C^{-1}$. Since the sapphire crystal has a trigonal structure of class ($3\,\bar{m}$), its stiffness matrix C, after omitting the repeated indices, becomes:

$$\begin{Bmatrix} \sigma_{xx} \\ \sigma_{yy} \\ \sigma_{zz} \\ \sigma_{yz} \\ \sigma_{zx} \\ \sigma_{xy} \end{Bmatrix} = \begin{bmatrix} C_{11} & C_{12} & C_{13} & C_{14} & 0 & 0 \\ C_{12} & C_{11} & C_{13} & -C_{14} & 0 & 0 \\ C_{13} & C_{13} & C_{33} & 0 & 0 & 0 \\ C_{14} & -C_{14} & 0 & C_{44} & 0 & 0 \\ 0 & 0 & 0 & 0 & C_{44} & C_{14} \\ 0 & 0 & 0 & 0 & C_{14} & 1/2(C_{11} - C_{12}) \end{bmatrix} \times \begin{Bmatrix} \varepsilon_{xx} \\ \varepsilon_{yy} \\ \varepsilon_{zz} \\ \gamma_{yz} \\ \gamma_{zx} \\ \gamma_{xy} \end{Bmatrix}, \tag{3}$$

where the tensorial stress and strain components are written in a vector form. In Eq. (3) C_{11} ($= C_{22}$) is related to the longitudinal distortions in the x_1-direction (respectively x_2-direction), and C_{33} is related to the longitudinal distortions in the x_3-direction. C_{44} relates to the shear distortion in the x_1–x_2 plane, and C_{12}, C_{13} and C_{14} relate to more complicated distortions. The values of C_{ij} are quite consistent in the literature. For example, $C_{11} = 4.968$ (10^{12} dynes/cm^2), $C_{33} = 4.981$, $C_{44} = 1.474$, $C_{13} = 1.57$, and $C_{14} = -0.22$ in [4]; $C_{11} = 497.6$ (GPa), $C_{12} = 162.6$, $C_{13} = 117.2$, $C_{14} = 22.9$, $C_{33} = 501.8$, and $C_{44} = 147.2$ in [5]; $C_{11} = 497.5$ (GPa), $C_{12} = 162.7$, $C_{13} = 115.5$, $C_{14} = 22.5$, $C_{33} = 503.3$, and $C_{44} = 147.4$ in [6]. Even though the independent elastic constants are only six, they are located in the elastic matrix in such a way that the material is not orthotropic in the coordinate system $x_1x_2x_3$, despite the three-fold symmetry of the crystal. If the small term C_{14} is neglected, however, the material becomes transversely isotropic, with the plane of

isotropy being plane x_1–x_2. The compliance matrix than takes the form of

$$[S] = \begin{bmatrix} \frac{1}{E_{xx}} & -\frac{\mu_{xy}}{E_{yy}} & -\frac{\mu_{xz}}{E_{zz}} & 0 & 0 & 0 \\ -\frac{\mu_{xy}}{E_{xx}} & \frac{1}{E_{yy}} & -\frac{\mu_{zy}}{E_{zz}} & 0 & 0 & 0 \\ -\frac{\mu_{xz}}{E_{xx}} & -\frac{\mu_{yz}}{E_{yy}} & \frac{1}{E_{zz}} & 0 & 0 & 0 \\ 0 & 0 & 0 & \frac{1}{G_{yz}} & 0 & 0 \\ 0 & 0 & 0 & 0 & \frac{1}{G_{xz}} & 0 \\ 0 & 0 & 0 & 0 & 0 & \frac{1}{G_{xy}} \end{bmatrix}. \quad (4)$$

If the elastic coefficients (GPa) are taken as $C_{11} = 497.6$, $C_{12} = 162.6$, $C_{13} = 117.2$, $C_{33} = 498.1$, $C_{44} = C_{55} = 147.2$, then from Eq. (4) the elastic moduli in coordinate system $x_1x_2x_3$ are calculated as $E_{x_1x_1} = E_{x_2x_2} = 1/S_{11} = 431.24$ GPa, $E_{x_3x_3} = 1/S_{33} = 456.49$ GPa, $G_{x_1x_2} = 1/S_{66} = 167.5$ GPa, $G_{x_1x_3} = G_{x_2x_3} = 1/S_{44} = 147.2$ GPa, $\mu_{x_1x_2} = \mu_{x_2x_1} = 0.2873$, $\mu_{x_1x_3} = \mu_{x_2x_3} = 0.1677$, $\mu_{x_3x_1} = \mu_{x_3x_2} = 0.1775$. Thus, a sapphire substrate in the c-plane (0 0 0 1) will be transversely isotropic, having in its plane $E = 431.24$ GPa, $\mu_{x_1x_2} = 0.2873$ GPa, and $G_{x_1x_2} = 1/S_{66} = 167.5$ GPa.

The R-plane sapphire wafer however is oriented in a plane different from the coordinate planes in the $x_1x_2x_3$ coordinate system. In order to calculate the in-plane material properties in the R-plane, the elastic matrix C has to be transformed into the new coordinate system XYZ by applying the rule for rotational transformation of a tensor of rank 4

$$C'_{ijkl} = R_{im}\, R_{jn}\, R_{kp}\, R_{lq}\, C_{mnpq}, \quad (5)$$

where R_{ij} is the transformation matrix that transforms the components of a vector from the coordinate system $x_1x_2x_3$ to the coordinate system XYZ. This requires the direction cosines of the new coordinate system with respect to the old coordinate system. For an R-plane wafer, the unit vectors of the new coordinate system XYZ are $\mathbf{i}^t_X = \{0.7309 - 0.4220 - 0.5363\}$, $\mathbf{i}^t_Y = \{-0.0251 - 0.8020 - 0.5968\}$ and $\mathbf{i}^t_Z = \{0.6820 - 0.4228 - 0.5968\}$. Both the elastic and compliance matrices in the XYZ coordinate system appear to lack zero terms; therefore the material is anisotropic in XYZ. Some terms however are small (less than 3% of the largest term $C'_{11} = 462.40$ GPa) and can be neglected: $C'_{14} = 1.50$ GPa, $C'_{15} = C'_{16} = 11.6$ GPa, $C'_{24} = C'_{34} = -8.75$ GPa, $C'_{25} = C'_{36} = -5.13$ GPa, $C'_{26} = C'_{35} = 7.86$ GPa, $C'_{45} = C'_{46} = -13.17$ GPa, and $C'_{56} = 10.44$ GPa. Thus, the material becomes orthotropic in the R-plane. Then the material constants are obtained as $E_{XX} = 386.00$ GPa, $E_{YY} = E_{ZZ} = 381.88$ GPa, $\mu_{XY} = \mu_{XZ} = 0.2478$, $\mu_{YX} = \mu_{ZX} = 0.2451$, $\mu_{YZ} = \mu_{ZY} = 0.2519$, $G_{XY} = G_{XZ} = 169.98$ GPa, and $G_{YZ} = 172.64$ GPa.

2.2. Thermal and other properties

There are various reports on the properties of sapphire, such as density, fracture toughness K_I, tensile strength, specific heat c_p, coefficient of thermal expansion α, and coefficient of conductivity k [7–16]. The density of sapphire is calculated as 3.983 (g cm^{-3}) in [13], and 3.96–3.98 (g cm^{-3}) on various web pages, e.g., [1–3,17]. The reports on the tensile strength are not very consistent: 300 MPa in [17,18], 250–400 MPa in [19]; and it is provided as a function of temperature in [2], i.e., 400 MPa at 25 °C, 275 at 500 °C, and 345 at 1000 °C. The fracture toughness (the critical intensity factor K_{Ic}) differs from one source to another: K_{Ic} is 2.0 (MPa m$^{1/2}$) in [18], 4.0 (MPa m$^{1/2}$) in [17] and 3.0–5.0 (MPa m$^{1/2}$) in [20].

The research outcome on the specific heat c_p of single crystal sapphire appears to be consistent, Fig. 3(a).

The values of the coefficient of thermal expansion, α (1 °C), also vary slightly from one report to another.

The linear coefficient of thermal expansion in [15] is given in a technical sense, i.e., α^*, which is defined as

$$\alpha* = \frac{(\mathrm{d}L/\mathrm{d}T)}{L_{293}}, \quad (6)$$

where L is the length, L_{293} is the length at room temperature (293 K), T is temperature. α^* can be used to calculate the true, or instantaneous, coefficient $\alpha = (\mathrm{d}L/\mathrm{d}T)/L$ as follows:

$$\alpha = \alpha * \left(\frac{1 + \Delta L}{L_{293}}\right)^{-1} \quad (7)$$

As shown in Fig. 3(b), α is direction-dependent, and two sets of data are provided, parallel to the c-axis, α_c, and perpendicular to the c-axis (that is parallel to the a-axis α_a), sapphire is transversely isotropic. Then, the thermal coefficient in an arbitrary direction, specified by its angle θ with respect to the c-axis, can be calculated [21] by

$$\alpha_\theta = \alpha_c \cos^2\theta + \alpha_a \sin^2\theta. \quad (8)$$

According to the published data, it appears that the coefficient of thermal conductivity of sapphire k depends slightly on the orientation, being higher along the c-axis, Fig. 3(c).

3. Heat transfer

An R-plane sapphire wafer of a diameter of 150 mm and a thickness of 0.6 mm was studied, Fig. 4.

The thermal material constants were chosen as recommended in [12,13], and the coefficient of thermal expansion α was adopted as for Linde synthetic sapphire [14]. The wafer was assumed subjected to the thermal history in Fig. 5.

The boundary conditions adopted here are similar to those previously used by the authors [22,23]: the single wafer is considered in thermal equilibrium with the surrounding wafers; the wafer is subjected to radiation on its edges while under high environmental temperature, but subjected to convection on the edges while at low room temperature; the environmental temperature is transferred from the edges through the wafer by heat

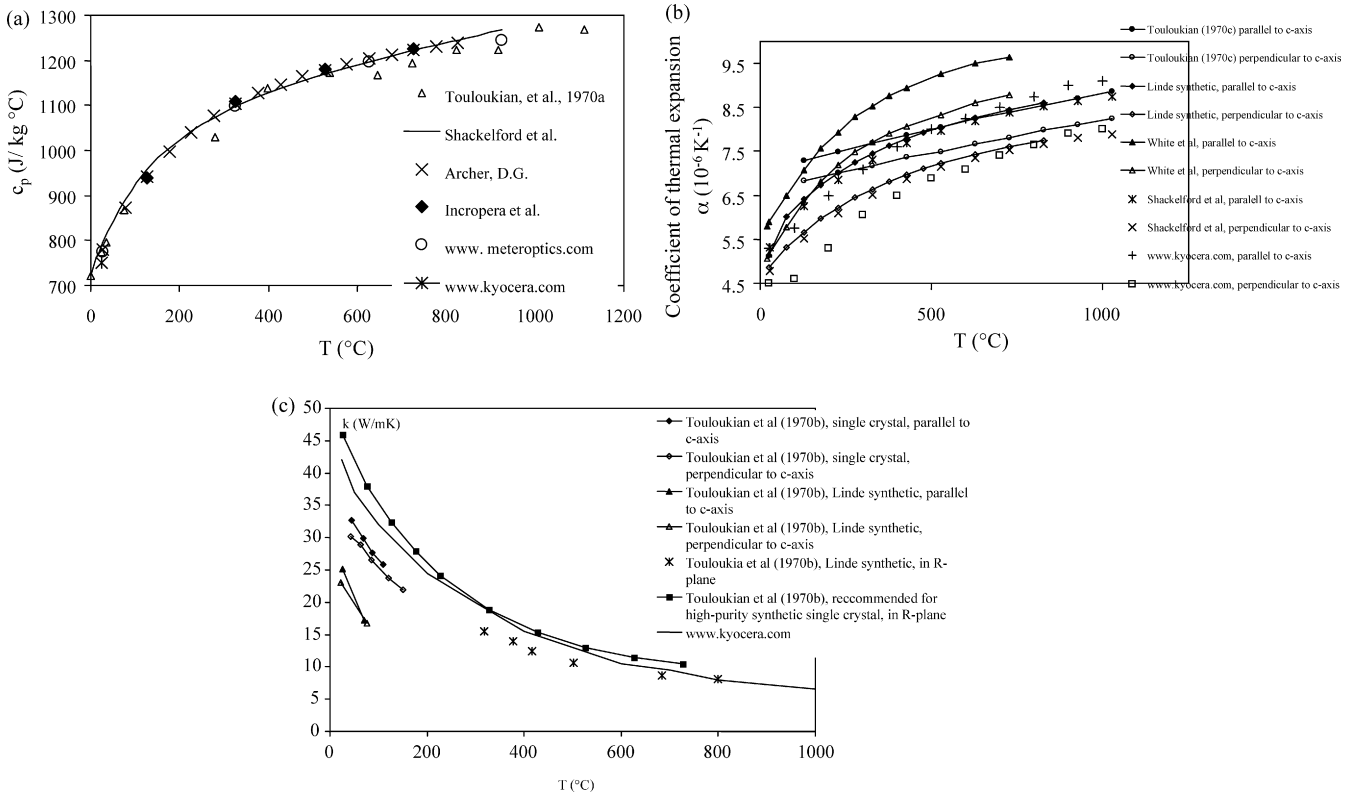

Fig. 3. (a) Variation of specific heat of single crystal sapphire, with temperature, (b) coefficient of thermal expansion α (1 °C) and (c) coefficient of thermal conductivity k (W/m K).

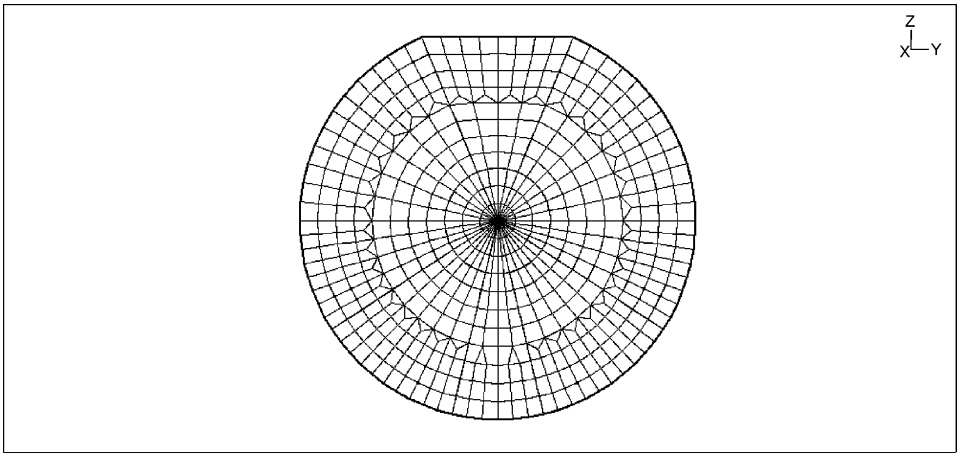

Fig. 4. FEA model in the thermal and stress analysis simulations.

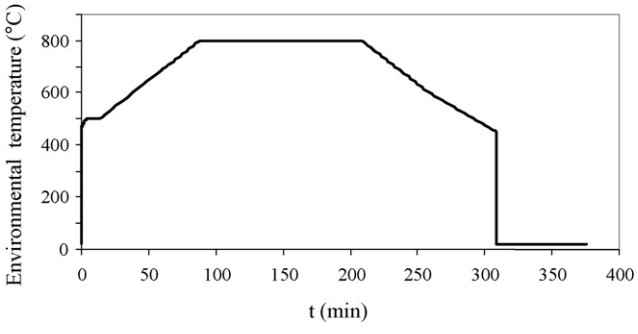

Fig. 5. Variation of environmental temperature with time.

conduction. Transient heat transfer analysis leads to the same temperature distribution for the anisotropic sapphire wafer, as for the isotropic sapphire wafer [22] because the sapphire thermal properties are not directional dependent, e.g., Figs. 6 and 7.

To check the temperature distribution obtained using FEA, a comparison was made with an approximate analytical solution based on the energy conservation principle. The check was performed in two cases: (1) for the transient radiation heat transfer at constant temperature of the surrounding $T_{sur} = 800$ °C, Fig. 5 and (2) for the transient convection heat transfer at room temperature $T_\infty = 20$ °C. The energy conservation principle states that for a control volume V, the increase in the stored energy

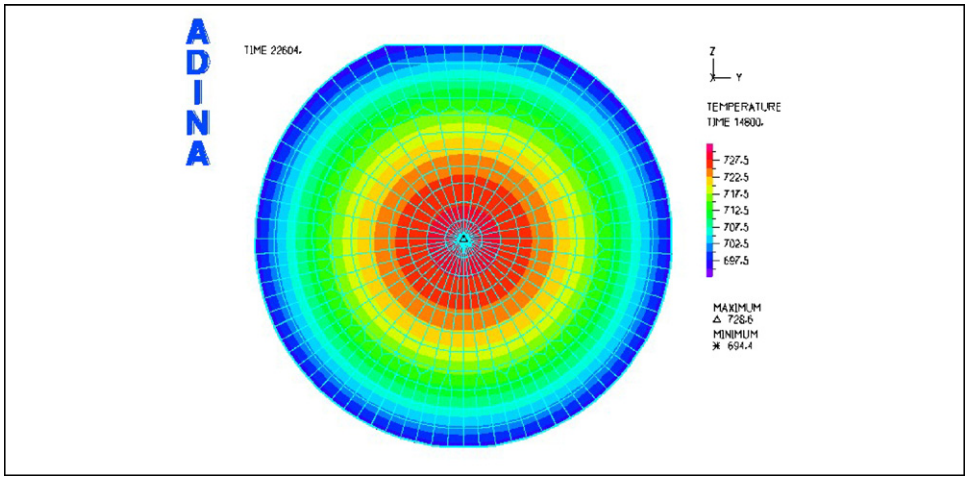

Fig. 6. Contour plot of the temperature across the wafer at time 246.7 min.

$\dot{E}_{st}$ equals the energy which enters the control volume $\dot{E}_{in}$ (zero in this case) minus the energy which leaves the control volume $\dot{E}_{out}$, i.e.,

$$\dot{E}_{in} - \dot{E}_{out} = \dot{E}_{st}. \tag{9}$$

In the case of radiation, the rate of the leaving energy is

$$\dot{E}^r_{out} = -\varepsilon\sigma A^r_s(T^4 - T^4_{sur}) \tag{10}$$

where A^r_s is the radiating surface, ε is the emissivity coefficient, $\sigma = 5.67 \times 10^{-8}$ W/(m^2 K^4) is the Stefan–Boltzmann constant, T is the temperature at time t, T_{sur} is the surrounding temperature, 800 °C.

In the case of convection,

$$\dot{E}^c_{out} = -hA^c_s(T - T_\infty) \tag{11}$$

where h is the convection coefficient, A^c_s is the convective surface, and $T_\infty = 20$ °C.

The rate of the stored energy in both cases is

$$\dot{E}_{st} = \frac{d}{dt}(\rho Vc) \tag{12}$$

where ρ is the sapphire density, $c = c_p$, V is the volume of the wafer. For constant T_{sur}, T_∞, h and c, Eqs. (9)–(12) can be solved for the temperature T at any instant of time t greater than the initial instant of time t_i, [24]. In the case of convection only,

$$T = T_\infty + (T_i - T_\infty)e^{-(hA^c_s/\rho Vc)(t-t_i)} \tag{13}$$

and in the case of radiation only,

$$t = \frac{\rho Vc}{4\varepsilon A^r_s\sigma T^3_{urs}}\left\{\ln\left|\frac{T_{sur}+T}{T_{sur}-T}\right| - \ln\left|\frac{T_{sur}+T_i}{T_{sur}-T_i}\right| + 2\left[\tan^{-1}\left(\frac{T}{T_{sur}}\right) - \tan^{-1}\left(\frac{T_i}{T_{sur}}\right)\right]\right\} \tag{14}$$

In the above equations, T is considered uniformly distributed in the wafer, h and c are constant. In the present study, this is not the case because T is non-uniform, h and c are temperature dependent, T_∞ and T_{sur} are varying in time. For a rough comparison however, it can be assumed that T is the average temperature between the wafer edge and wafer centre; h and c can also be taken as average values.

The FEA results are compared with the approximate results in the case of the radial radiation at time $t_i = 88.33$ min, after which the surrounding temperature is held constant at $T_{sur} = 800$ °C. The increment of time is denoted by Δt and measured from t_i. Fig. 8 shows that the average wafer temperature increases from 675.9 to 800 °C for around 120 min in the FEA simulations, and for around 71 min using Eq. (14).

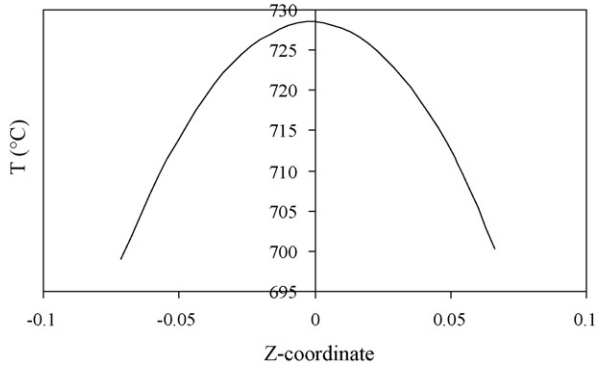

Fig. 7. Temperature along the vertical wafer diameter at time 246.7 min.

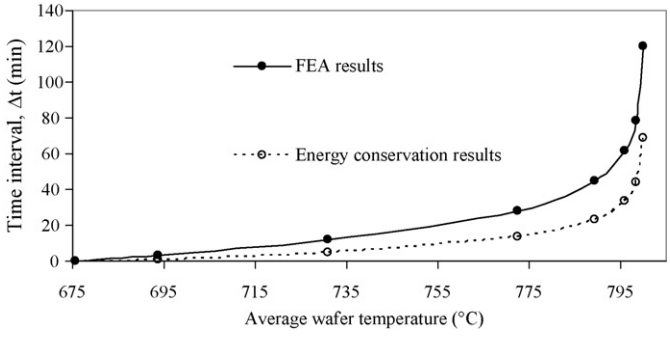

Fig. 8. Δt vs. the wafer temperature T. Δt (min) is the time interval after the point t_i, at which the surrounding temperature is held constant at 800 °C. T (°C) is the average wafer temperature reached at time $t_i + \Delta t$.

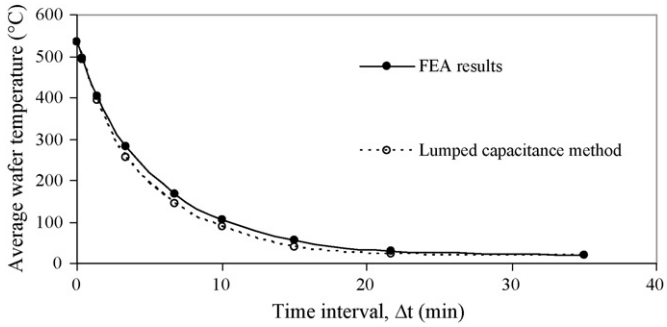

Fig. 9. The wafer temperature T vs. Δt. Δt (min) is the time interval after the point $t_i = 308.3$ min, at which the wafer is placed at room temperature. T (°C) is the average wafer temperature reached at time $t_i + \Delta t$.

Another comparison is made for the cooling of the wafer at room temperature of $T_\infty = 20\,^\circ$C. In the simulations, only convection on the edges and on the front wafer surface was taken into account. Fig. 9 illustrates how the average wafer temperature decreases with the time upon cooling at room temperature; obviously the results are very close.

4. Thermal stresses

In the present study, the thermal stress analysis on the anisotropic sapphire was performed for a non-linear thermo-elastic orthotropic material. The values of E, μ and α were supplied to the software in the material coordinate system $x_1x_2x_3$, and the direction cosines of the material axes x_1, x_2 and x_3 were provided with respect to the XYZ coordinate system. The stress analysis shows that the wafer is in an almost axisymmetric and plane stress state. The principal stresses are in the radial and circumferential direction in the plane of the wafer. Of them, the largest tensile stress is of prime importance as it can induce fracture failure. The highest tensile stress appears in the middle of the flat edge, at time $t = 246.7$ min during cooling down, when $\sigma_{YY} = 108.2$ MPa, Fig. 10(a). This figure also shows the stress variation of the circumferential stresses at three more points, with time, trough the whole thermal history.

It can be seen that the circumferential stresses along the edge are negative on heating up and positive during cooling down, whereas at the wafer centre the radial stress has an opposite sign, e.g., Fig. 10(a and b). The largest tension σ_{11} at the bottom edge and on the sides are lower that at the top flat edge, around 54 MPa.

5. Fracture in an *R*-plane wafer

Single crystal sapphire is not defect-free, some small cracks or flaws can exist in a wafer, such as those induced by polishing along the edges. It is essential for the process design to predict whether the initial defects will grow and lead to a fracture failure, or the defects will be stable. There are several fracture theories that study the stability of an existing crack and its propagation, e.g., [25]. In these studies, a crack is assumed in the most dangerous site and an analysis for the current load is performed to establish a characteristic quantity that will define the

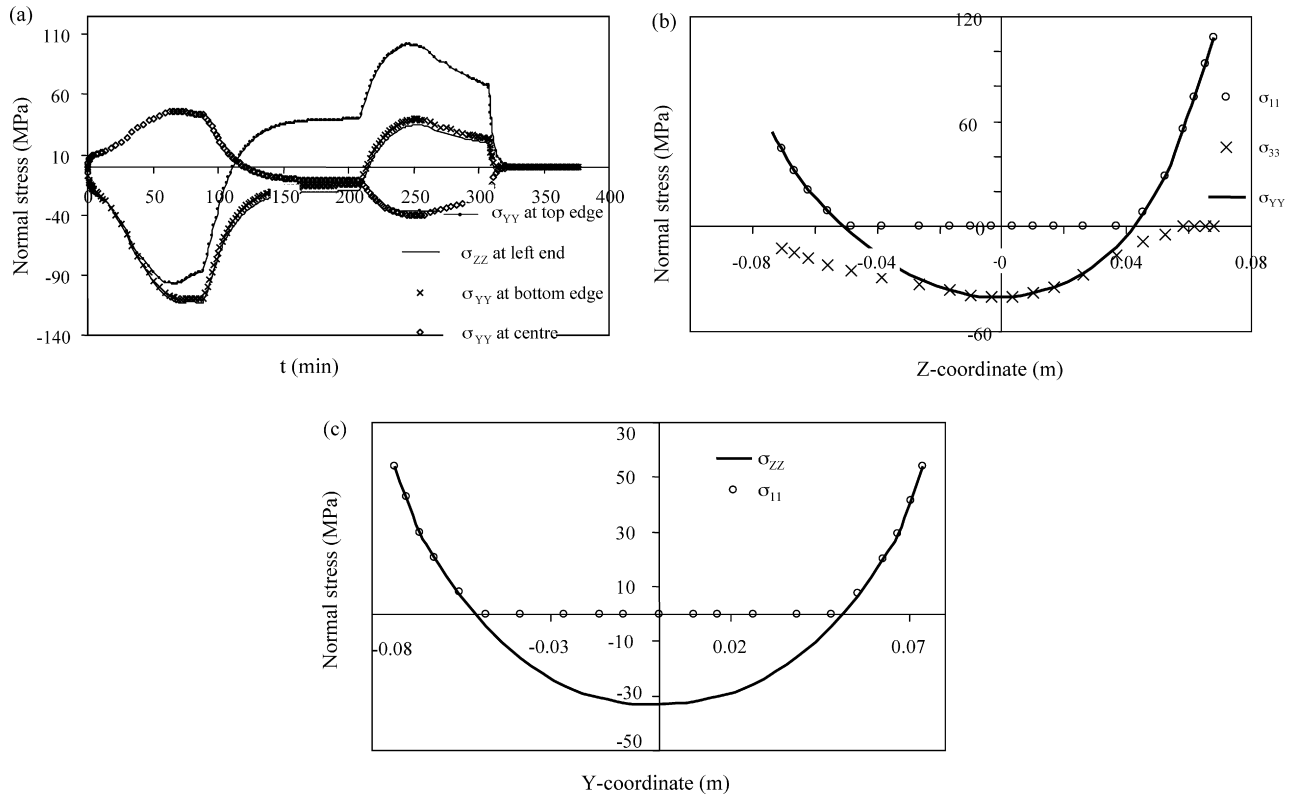

Fig. 10. (a) Variation of the normal stress with time at four locations in the wafer, (b) normal stress distribution in the sapphire wafer along the vertical diameter, at time 246.7 min and (c) normal stress distribution in the sapphire wafer along the horizontal diameter, at time 246.7 min.

tendency of the crack to extend. This quantity is compared with an experimentally determined critical value, which measures the material fracture toughness corresponding to the onset of unstable fracture process.

The following two fracture theories will be used in the present paper: (1) the maximum tensile stress criterion states that fracture in an opening mode occurs at the point and in the direction of the maximum tensile stress σ_0, when σ_0 reaches the critical value of $\sigma_{0c} = (EG_c/\pi a)^{1/2}$ (according to Griffith theory), where a is the length of the pre-existing crack, γ is the energy required to form a unit of a new material surface (fracture surface energy), and $G_c = 2\gamma$ is the energy available for crack growth (fracture energy release rate). (2) The maximum stress intensity factor K_I theory states that fracture in an opening mode initiates when K_I at the crack tip reaches its critical value of $K_{Ic} = (EG_c)^{1/2}$.

While for isotropic materials, stress- and energy-based fracture criteria lead to similar results, for anisotropic materials this is not so. Anisotropic materials have directional preferences—they are stronger in some directions and weaker in others. Moreover, single crystal materials have a discrete number of cleavage planes and do not always fracture in the direction of the highest tensile stress, but rather in the direction where a high tensile stress acts on a weak cleavage plane. This was supported experimentally [26] and the results on notched A-plane sapphire specimens showed that the energy criterion fails to predict the fracture path of most of the specimens. A dimensionless parameter A was introduced to measure the onset of crack initiation. In a notched sample $A^{(N)} = \sigma_{\xi\xi}\,(2\pi R_0/\gamma_\lambda E_{\xi\xi})^{1/2}$ where R_0 is the notch radius, σ_ξ and E_ξ are the tensile stress and Young's modulus in a direction ξ perpendicular to a cleavage plane λ, and γ_λ is the fracture surface energy of cleavage plane λ. The crack appeared at a point and in a direction where $A^{(N)}$ was maximum. For specimens with pre-existing cracks, the crack kinked in the direction where $A^{(c)} = K_{I\xi}/(\gamma_\lambda E_{\xi\xi})^{1/2}$ was maximum, where K_I is the stress intensity factor in the direction perpendicular to the cleavage plane. It was also shown that the fracture planes are actually the weakest families of cleavage planes, i.e., $\{\bar{1}\,0\,1\,2\}$ and $\{1\,0\,\bar{1}\,0\}$.

It is evident that in anisotropic materials σ_{0c} and K_{Ic} depend on γ_λ of the cleavage plane along which the crack propagates. Reports on γ_λ of different cleavage planes in single crystal sapphire [26] show that the strongest plane is the basal c-plane $(0\,0\,0\,1)$ having $\gamma_\lambda > 40\,\mathrm{J/m^2}$, and the weakest family of planes is $\{\bar{1}\,0\,1\,2\}$ having $\gamma_\lambda = 6\,\mathrm{J/m^2}$. The other families of cleavage planes are stronger: $\{\bar{1}\,\bar{1}\,2\,6\}$ with $\gamma_\lambda = 24.2\,\mathrm{J/m^2}$ and $\{1\,0\,\bar{1}\,0\}$ with $\gamma_\lambda = 7.3\,\mathrm{J/m^2}$. With these values of γ_λ, the critical stress intensity factor on a cleavage plane λ can be calculated as $K_{Ic} = (2E_{\xi\xi}\gamma_\lambda)^{1/2}$. However, the Young's modulus in a direction normal to a cleavage plane $E_{\xi\xi}$ needs to be determined first, using the transformation rule of Eq. (5). This requires the direction cosines of the cleavage plane, which can be calculated using coordinate geometry, in the following way. An arbitrary plane has an equation in the xyz coordinate system of the form

$$\frac{x}{A} + \frac{y}{B} + \frac{z}{C} = 1 \tag{15}$$

where A, B and C are the intercepts of the plane with the x, y and z axes, respectively.

The above equation can be re-arranged as

$$a_1 x + b_1 y + c_1 z - 1 = 0, \tag{16}$$

where $a_1 = 1/A$, $b_1 = 1/B$ and $c_1 = 1/C$ are also the coordinates of a vector normal to the plane. The direction cosines of this vector with respect to x, y and z can be calculated as

$$l = \frac{a_1}{\sqrt{a_1^2 + b_1^2 + c_1^2}}$$
$$m = \frac{b_1}{\sqrt{a_1^2 + b_1^2 + c_1^2}}. \tag{17}$$
$$n = \frac{c_1}{\sqrt{a_1^2 + b_1^2 + c_1^2}}$$

The elastic modulus of sapphire along that normal vector is also needed; it can be found through the elastic constants in coordinate system $\xi\eta\zeta$, which includes the cleavage plane and two more normal planes. Let the cleavage plane be denoted by λ, the direction of its normal vector by ξ, and the other two normal vectors by η and ζ. After transforming the elastic matrix C from the xyz coordinate system into the $\xi\eta\zeta$ coordinate system, the Young's modulus along the three normal vectors can be calculated as $E_{\xi\xi} = 1/S(1,1)$, $E_{\eta\eta} = 1/S(2,2)$ and $E_{\zeta\zeta} = 1/S(3,3)$. The results for all cleavage planes are summarized in Table 1 below. Note that $a = 4.758$ Å is the lattice constant (Fig. 1) and $c = 12.991$ Å is the crystal dimension along the optical c-axis. Table 1 also lists the surface energy γ_λ [26] and the critical fracture toughness K_{Ic} on all cleavage planes.

With known Young's modulus perpendicular to cleavage plane λ, one can assess the stability of a pre-existing crack located in that plane, by applying the fracture theories. They all require however a characteristic value that measures the stress state, for example, the maximum tensile stress σ_0 in the ξ-direction. An assumption was made that a pre-existing crack $BCC''B''$ in an arbitrary cleavage plane λ is located at an arbitrary point along the wafer edge, Fig. 11 (point B is in the wafer face).

The crack has an initial length $a = BB''$. Point B is specified by angle δ, which is the angle between the Y-axis and the radius-vector of point B. The cleavage plane makes an angle λ with the wafer plane, and intersects the wafer face at line AB making an angle α with the Y-axis. If the magnitude of the tensile stress normal to the cleavage plane $\sigma_{\xi\xi}$ is higher than the critical value necessary to break the inter-atomic bonds in the cleavage plane, the crack will be unstable and will propagate in the BA direction. In order to find $\sigma_{\xi\xi}$, first the tensile stress σ_{nn} has to be calculated in a direction normal to the intersection of the wafer plane and the cleavage plane, line AB, and then, the tensile stress component $\sigma_{\xi\xi}$ can be obtained.

Thus, the line of intersection of the wafer plane with cleavage plane λ, i.e., line BA, needs to be determined first, and then the angle between the wafer plane and cleavage plane, λ. The wafer

Table 1
Young's modulus, surface fracture energies, and K_{IC}, for various cleavage planes

Cleavage plane ξ	$(1\,1\,\bar{2}\,0)$	$(1\,\bar{1}\,0\,0)$	$(0\,1\,\bar{1}\,0)$	$(0\,0\,0\,1)$
Intercepts with *x*, *y*, *z* axes				
a_λ	a	a	∞	∞
b_λ	2.74	−8.24	4.12	∞
c_λ	∞	∞	∞	12.991
$E_{\xi\xi}$ (GPa)	431.2	431.2	431.2	456.5
γ_λ (J/m^2)	7.3	7.3	7.3	40
K_{Ic} (MPa m$^{1/2}$)	2.509	2.509	2.509	6.043

Cleavage plane ξ	$(1\,0\,\bar{1}\,0)$	$(0\,\bar{1}\,1\,0)$	$(1\,\bar{2}\,1\,6)$	$(1\,1\,\bar{2}\,6)$
Intercepts with *x*, *y*, *z* axes				
a_λ	a	∞	a	a
b_λ	8.24	−4.121	−2.74	2.74
c_λ	∞	∞	$c/6$	$c/6$
$E_{\xi\xi}$ (GPa)	431.2	431.2	381.4	381.4
γ_λ (J/m^2)	7.3	7.3	24.4	24.4
K_{Ic} (MPa m$^{1/2}$)	2.509	2.509	4.314	4.314

Cleavage plane ξ	$(2\,\bar{1}\,\bar{1}\,6)$	$(\bar{1}\,\bar{1}\,2\,6)$	$(\bar{1}\,2\,\bar{1}\,6)$	$(\bar{2}\,1\,1\,6)$
Intercepts with *x*, *y*, *z* axes				
a_λ	$a/2$	$-a$	$-a$	$-a/2$
b_λ	∞	−2.74	2.74	∞
c_λ	$c/6$	$c/6$	$c/6$	$c/6$
$E_{\xi\xi}$ (GPa)	381.4	381.4	381.4	381.4
γ_λ (J/m^2)	24.4	24.4	24.4	24.4
K_{Ic} (MPa m$^{1/2}$)	4.314	4.314	4.314	4.314

Cleavage plane ξ	$(\bar{1}\,0\,1\,2)$	$(1\,0\,\bar{1}\,2)$	$(0\,\bar{1}\,1\,2)$	$(\bar{1}\,1\,0\,2)$	$(0\,1\,\bar{1}\,2)$
Intercepts with *x*, *y*, *z* axes					
a_λ	$-a$	a	∞	$-a$	∞
b_λ	−8.24	8.24	$-a\cos(30)$	8.24	$a\cos(30)$
c_λ	$c/2$	$c/2$	$c/2$	$c/2$	$c/2$
$E_{\xi\xi}$ (GPa)	386.1	386.1	386.1	386.1	386.1
γ_λ (J/m^2)	6	6	6	6	6
K_{Ic} (MPa m$^{1/2}$)	2.152	2.152	2.152	2.152	2.152

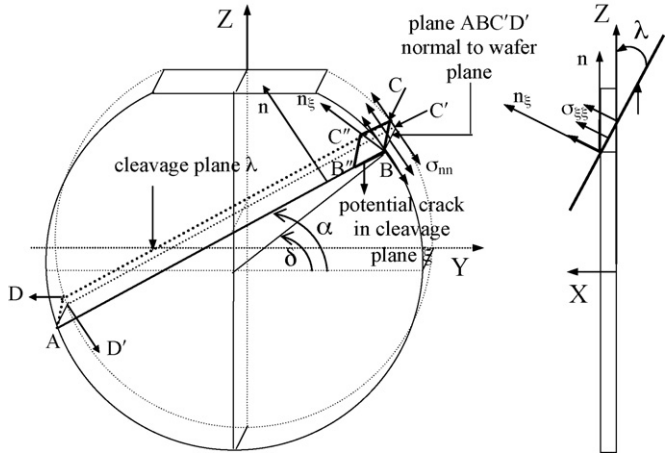

Fig. 11. An arbitrary cleavage plane λ intersecting the wafer plane at plane *ABCD*; λ is the angle of inclination of plane λ to the wafer plane; plane *ABC′D′* is normal to the wafer plane; α is the angle between the intersection line *AB* (or *CD*) and the *Y*-axis; *n* is the normal to plane *ABC′D′*; n_ξ is the normal to the cleavage plane λ; σ_{nn} is the tensile stress acting normal to plane *ABC′D′*; $\sigma_{\xi\xi}$ is the tensile stress in the ξ-direction acting normal to the cleavage plane λ.

plane can be described by Eq. (16):

$$a_2x + b_2y + c_2z - 1 = 0. \tag{18}$$

where a_2, b_2 and c_2 are the coordinates of a vector normal to the *R*-plane. They can be found from the intercepts of the *R*-plane with the *x*, *y* and *z* coordinate axes ($a_R = 4.758$ Å, $b_R = -8.241$ Å and $c_R = c/2 = 6.496$ Å), and are calculated as 0.21, −0.121 and 0.154, respectively. The intersection line *AB* can than be defined by a vector collinear to it. That collinear vector can be calculated as the vector product of the two vectors that are normal to the *R*-plane and the cleavage plane. In the *xyz* coordinate system, this reads:

$$\begin{vmatrix} \vec{i} & \vec{j} & \vec{k} \\ a_1 & b_1 & c_1 \\ a_2 & b_2 & c_2 \end{vmatrix} = (b_1c_2 - b_2c_1)\vec{i} + (a_2c_1 - a_1c_2)\vec{j} + (a_1b_2 - a_2b_1)\vec{k} = p\vec{i} + q\vec{j} + r\vec{k} \tag{19}$$

where $\vec{i}$, $\vec{j}$and $\vec{k}$ are the unit vectors of the *x*, *y* and *z* coordinate axes, respectively, and *p*, *q* and *r* are the coordinates of the collinear vector in the *xyz* coordinate system. Moreover, the *Y*-axis has directional cosines of $l_Y = -0.0251$, $m_Y = -0.802$ and $n_Y = -0.5968$. Thus, α can be found from

$$\cos\alpha = \frac{pl_Y + qm_Y + rn_Y}{\sqrt{(p^2 + q^2 + r^2)(l_Y^2 + m_Y^2 + n_Y^2)}} \tag{20}$$

Eq. (20) leads to two angles, α and $-\alpha$, having the same directional cosine. In order to define which is the right angle, also necessary is to calculate the angle between the intersection and the *Z*-axis, with the direction cosines of the *Z*-axis in the *xyz* coordinate system being $l_Z = 0.682$, $m_Z = 0.423$ and $n_Z = -0.597$. In a similar way, the intersections of all cleavage planes with the wafer plane are located, and the results are presented in Table 2 and Fig. 12.

Further, the angle between the wafer plane and cleavage plane λ needs to be also determined. To do this, Eq. (20) can be applied if $p = a_1$, $q = b_1$ and $r = c_1$ (the normal vector to the cleavage plane), and l_Y is substituted with a_2, m_Y with b_2, and n_Y with c_2, respectively (the normal vector to the *R*-plane). The results are provided in Table 2 for all cleavage planes. With the data in Tables 1 and 2, one can now find K_I and $\sigma_{\xi\xi}$ at the point of the pre-existing crack, due to the applied load, and apply the maximum tensile stress or the maximum stress intensity factor fracture theories. As already mentioned, the FEA simulations showed that the largest tensile stress occurred at the wafer edge during cooling down; therefore a crack is expected to initiate from there. If the stress components at a particular point are denoted by σ_{YY}, σ_{ZZ} and σ_{YZ}, the stress component normal to line *AB*, σ_{nn}, is calculated as for a plane stress case:

$$\sigma_{nn} = \frac{\sigma_{YY} + \sigma_{ZZ}}{2} + \frac{\sigma_{YY} - \sigma_{ZZ}}{2}\cos 2(\alpha + \pi/2) + \sigma_{YZ}\sin 2(\alpha + \pi/2). \tag{21}$$

The stress component $\sigma_{\xi\xi}$ then becomes:

$$\sigma_{\xi\xi} = \sigma_{nn}\sin^2\lambda. \tag{22}$$

Table 2
Angles α and λ for various cleavage planes

Cleavage plane λ	Angle between the intersection of cleavage plane and R-lane, α (°), measured from the Y-axis, Fig. 2(a)	Angle between the cleavage plane and wafer plane (R-plane), λ (°)	Surface energy, γ_λ (J/m^2)	Critical fracture toughness, K_{Ic} (MPa m$^{1/2}$)	Young's modulus in the direction perpendicular to cleavage plane, $E_{\xi\xi}$
(0 0 0 1)	135	57.6	40	6.043	456.49
(1 $\bar{1}$ 0 0)	135	32.4	7.3	2.509	431.24
(1 0 $\bar{1}$ 0)	27.8	65.0	7.3	2.509	431.24
(0 $\bar{1}$ 1 0)	62.2	65.0	7.3	2.509	431.24
(01 $\bar{1}$ 0)	62.2	115.0	7.3	2.509	431.24
(1 $\bar{2}$ 1 6)	2.1	27.3	24.4	4.314	381.39
(1 1 $\bar{2}$ 6)	87.9	66.7	24.4	4.314	381.39
(2 $\bar{1}$ $\bar{1}$ 6)	87.9	27.3	24.4	4.313	381.39
($\bar{1}$ $\bar{1}$ 2 6)	2.1	66.7	24.4	4.313	381.39
($\bar{1}$ 2 $\bar{1}$ 6)	115.2	95.5	24.4	4.314	381.39
($\bar{2}$ 1 1 6)	154.8	95.5	24.4	4.314	381.39
($\bar{1}$ 0 1 2)	2.1	94.0	6	2.152	386.06
(1 0 $\bar{1}$ 2)	62.2	50.0	6	2.152	386.06
(0 $\bar{1}$ 1 2)	27.8	50.0	6	2.152	386.06
($\bar{1}$ 1 0 2)	135	115.2	6	2.152	386.06
(0 1 $\bar{1}$ 2)	87.9	94.0	6	2.152	386.06

Except for the flat top part, the stress state in the wafer is axisymmetric and Eq. (21) can be simplified bearing in mind that the circumferential stress is the first principal stress:

$$\sigma_{nn} = \frac{\sigma_{11}}{2}(1 + \cos 2(\alpha - \delta)). \tag{23}$$

As mentioned in Section 3, the maximum tensile stresses on the wafer edge appeared at time $t = 246.7$ min. At that point of time, Eqs. (21)–(23) are applied to a large number of points along the wafer edge, and $\sigma_{\xi\xi}$ is calculated on all cleavage planes passing through the points. Of all $\sigma_{\xi\xi}$ at a point, one is the maximum one, σ_0, acting on a cleavage plane making the largest angle λ with the wafer plane. The stresses σ_0 for a large number of points around the wafer edge and the corresponding cleavage planes are found, and plotted in Fig. 13(a), in order to locate the point most likely to fracture under the thermal load.

It is obvious that the largest value of $\sigma_0 = 107.5$ MPa occurs at the midpoint of the top flat edge, i.e., point 4 in Fig. 13(a), and is perpendicular to cleavage plane (0 1 $\bar{1}$ 2) having $\alpha = 87.9°$ and $\lambda = 94.0°$. According to the maximum tensile stress fracture theory, that point is most likely to fracture first, then points 5 and 4 at the top edge. The least likely points to fracture are point 2 and 6, located close to the top edge, where the principal stress σ_{11} is lowest. At the bottom part of the wafer, the stress state is axisymmetric and σ_{11} is of the same magnitude; despite that σ_0 is different due to the discrete nature of the cleavage planes.

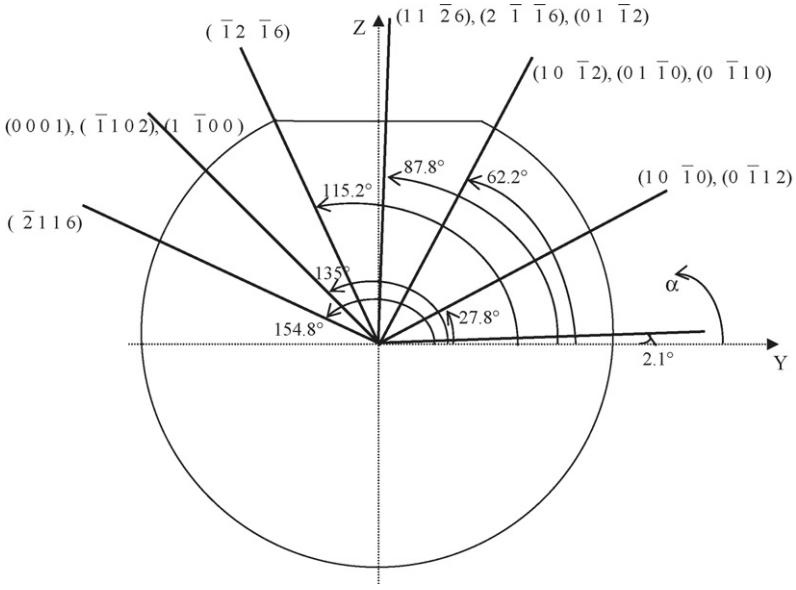

Fig. 12. Intersections of various cleavage planes and the wafer.

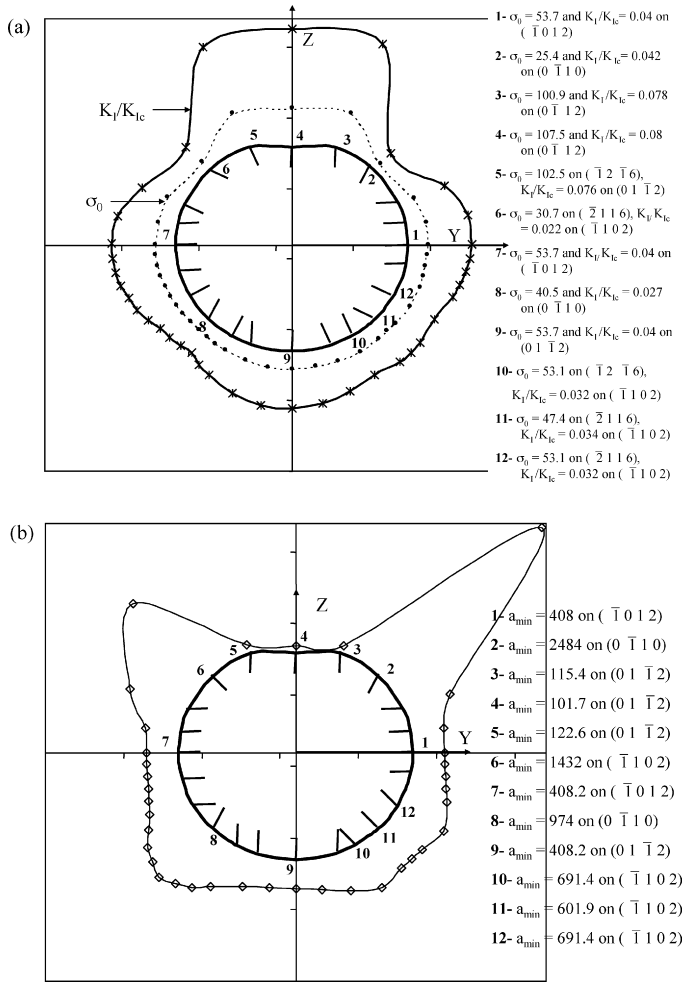

Fig. 13. (a) Distribution of σ_0 and max K_I/K_{Ic} along the wafer edge. Short lines denote the crack direction according to the σ_0 criterion and (b) distribution of a_{min} along the wafer edge. Short lines denote the crack direction.

Another way of locating the weakest and strongest points along the wafer circumference is by calculating the stress intensity factor K_I for the tensile stress $\sigma_{\xi\xi}$ on each cleavage plane, and then comparing it with the critical value K_{Ic}. K_I can be determined as for a semi-infinite plate subjected to a uniform tensile stress field, having an edge through crack under tension, e.g., [25]:

$$K_I = 1.12\sigma_{\xi\xi}(\pi a)^{1/2}. \quad (24)$$

K_{Ic} has already been calculated and listed in Table 1 for all cleavage planes. It will be reasonable however, if the ratio K_I/K_{Ic} is used instead. Thus, among all cleavage planes passing through the material point, the one having the largest ratio K_I/K_{Ic} will be the weakest. These calculations are performed for a number of points along the wafer circumference, for assumed $a = 0.7\,\mu m$. Then, the distribution of the largest ratios K_I/K_{Ic} as well as the crack direction according to the σ_0 criterion, are plotted in Fig. 13(a). At points where the weakest cleavage planes are different for the σ_0 and K_I/K_{Ic} criteria, both planes are listed in the legend. If K_{Ic} was the same for all cleavage planes, both fracture criteria would have provided the same results; however, the anisotropy of single crystal sapphire leads to different results. This is due to the fact that the σ_0 criterion dos not account for the different resistance of the different cleavage planes to fracture, while the K_I/K_{Ic} criterion does.

Another fracture criterion that would provide the weakest and strongest points along the wafer circumference is the minimum critical length a_{min} that would initiate an unstable crack in a particular cleavage plane. At a particular point along the edge, and in a particular cleavage plane, a critical crack length a_c can be calculated, which if exceeded by the pre-existing crack, the crack will propagate. The value of a_c can be determined for the critical toughness K_{Ic} on cleavage plane λ and the stress component $\sigma_{\xi\xi}$ normal to λ, using Eq. (24):

$$a_c = \frac{K_{Ic}^2}{(1.12^2\pi\sigma_{\xi\xi}^2)}. \quad (25)$$

Thus, for each cleavage planes λ passing through a point, a critical crack length a_c exists. Among all critical crack lengths a_c at the point, one is minimal, a_{min}. This crack is most likely to occur and it will be caused by a combination of a large tensile stress component $\sigma_{\xi\xi}$, and a weak plane λ having a small K_{Ic}. This criterion is obviously inverse to the K_I/K_{Ic} criterion because it will provide the minimum value of a_c where K_I/K_{Ic} is maximum. Fig. 13(b) below confirms that. The weakest point according to the a_{min} criterion is again at the middle of the flat edge, and the strongest is at $\alpha = 45^\circ$. If there is any source of stress concentration causing additional tensile stresses, it will increase the chance of wafer breakage. Stress concentration at the locations of the weak points should be avoided, and the stress concentration factors should be located at the strongest points instead.

The present study also considered the fracture phenomenon in a circular wafer subjected to the same thermal loading, in order to determine the influence of the anisotropic nature of the sapphire wafer. The first principal stress is circumferential, and has the same magnitude at all points, $\sigma_{11} = 54$ MPa. The results for σ_0 and a_{min} are presented in Fig. 14 below.

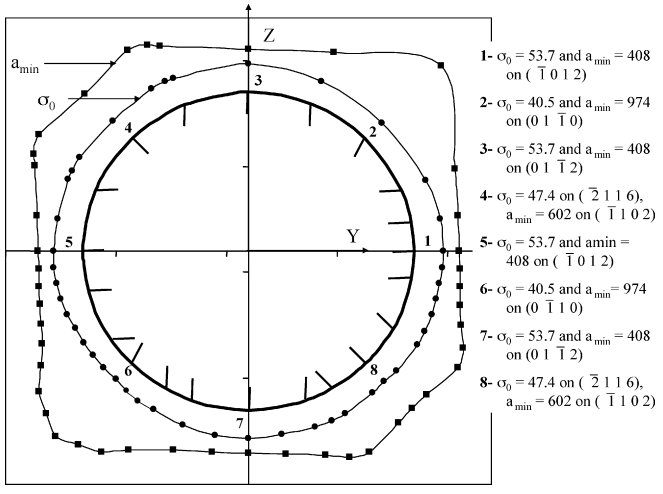

Fig. 14. Distribution of σ_0 and a_{min} along the edge of a circular wafer. Short lines denote the crack direction according to the a_{min} criterion.

If the circular wafer was made of isotropic material, which could break in the plane of the maximum tensile stress, both graphs in Fig. 14 would have been circular, and the crack direction would have been perpendicular to the wafer edge. Since sapphire is anisotropic and the cleavage planes have different fracture surface energies, even though the problem is axisymmetric, the fracture planes are not always perpendicular to the edge, and the critical crack length is not the same for all cleavage planes. It is obvious that the graphs in Fig. 14 are symmetric about the axes having $\alpha = 45^\circ$ (the image of the *c*-plane) and $\alpha = 135^\circ$ (the *a*-axis). The strongest points (2 and 6) are the ones along the image of the *c*-axis, which has $\alpha = 45^\circ$. The weakest points (1, 3, 5 and 7) are at $\pm 45^\circ$ to the image of the *c*-axis, and at $\pm 45^\circ$ to the *a*-axis; the latter has $\alpha = -45^\circ$. The point at the *a*-axis (point 4 and 8) are of intermediate strength.

6. Conclusions

The present study shows that:

1. An *R*-plane wafer made of single crystal sapphire can be considered orthotropic in its plane, and perpendicular to it.
2. *R*-plane sapphire wafers have been found to fracture under thermal shocks, predominantly perpendicular to the flat edge. This fracture behaviour can be explained with a high level of tensile stresses acting on a weak cleavage plane.
3. To account for the anisotropy, a modified maximum stress intensity factor criterion can be used, i.e., the maximum stress intensity factor ratio K_I/K_{Ic} criterion and its equivalent minimum critical crack length a_{min} criterion. Both criteria predict the crack at the flat edge to propagate in the weakest plane $(0\,1\,\bar{1}\,2)$.
4. It was also found that the points at the sides of the flat edge are the strongest and least prone to fracture. The influence of sapphire anisotropy on its fracture behaviour can be clearly seen in a circular wafer subjected to the same thermal loading. The strongest points are located along the image of the *c*-axis, and the weakest points are at 45° to the image of the *c*-axis and to the *a*-axis.

Acknowledgements

This work was supported by an ARC Linkage grant and Peregrine Semiconductor Australia.

References

[1] http://www.kyocera.com.
[2] http://www.mkt-intl.com/sapphires.
[3] http://www.sapphirewafers.com.
[4] W.G. Mayer, P.M. Parker, Method for the determination of elastic constants of trigonal crystal systems, Acta Crystallogr. 14 (1961) 725.
[5] J.M. Winey, Y.M. Gupta, r-Axis sound speed and elastic properties of sapphire single crystals, J. Appl. Phys. 90 (6) (2001) 3109.
[6] J.R. Gladden, J.H. So, J.D. Maynard, P.W. Saxe, Y.L. Page, Reconciliation of ab initio theory and experimental elastic properties of Al_2O_3, J. Appl. Phys. Lett. 85 (3) (2004) 392.
[7] D.G. Archer, Thermodynamic properties of synthetic sapphire (alpha-Al_2O_3), standard reference material 720 and the effect of temperature-scale differences on thermodynamic properties, J. Phys. Chem. Ref. Data 22 (6) (1993) 1441–1453.
[8] M.W. Chase, NIST-JANAF Thermochemical Tables, American Institute of Physics for the National Institute of Standards and Technology, 1998.
[9] D.A. Ditmars, S. Ishihara, S.S. Chang, G. Bernstein, Enthalpy and heat-capacity standard reference material: synthetic sapphires (alpha-Al_2O_3) from 10 to 2250 K, J. Res. Natl. Bureau Stand.–A. Phys. Chem. 87 (2) (1982) 159–163.
[10] J. Shackelford, W. Alexander, CRC Material Science and Engineering Handbook, CRC Press, 1992.
[11] R.W. Touloukian, Thermophysical Properties of Matter: the TPRC Data Series; a Comprehensive Compilation of Data, 1967.
[12] Y.S.E. Touloukian, R.W. Powel, C.Y. Ho, P.G. Klemens, Specific Heat Nonmetallic solids, IFI/PLENUM, New York-Washington, 1970.
[13] Y.S.E. Touloukian, R.W. Powel, C.Y. Ho, P.G. Klemens, Thermal Conductivity Nonmetallic solids, IFI/PLENUM, New York-Washington, 1970.
[14] Y.S.E. Touloukian, R.W. Powel, C.Y. Ho, P.G. Klemens, Thermal Expansion Nonmetallic solids, IFI/PLENUM, New York-Washington, 1970.
[15] G.K. White, M.L. Minges, Thermophysical Properties of Some Key Solids, CODATA Bulletin, International Council of Scientific Unions Committee on Data for Science and Technology, 1985.
[16] C.L. Yaws, Chemical Properties handbook, McGraw-Hill, New York, 1999.
[17] http://www.matweb.com.
[18] http://www.guildoptics.com.
[19] http://www.goodfellow.com.
[20] http://www.efunda.com.
[21] H.Y.B. Mar, W.D. Scott, Fracture induced in Al_2O_3 bycrystals by anisotropic thermal expansion, J. Am. Ceram. Soc. 53 (10) (1970) 555–558.
[22] T. Vodenitcharova, L.C. Zhang, I. Zarudi, Y. Yin, H. Domyo, T. Ho, Transient thermal analysis of sapphire wafers subjected to thermal shocks, IEEE Trans. Semicond. Manuf. 19 (3) (2006) 292–297.
[23] T. Vodenitcharova, L.C. Zhang, I. Zarudi, Y. Yin, H. Domyo, T. Ho, The effect of thermal shocks on the stresses in a sapphire wafer, IEEE Trans. Semicond. Manuf. 19 (4) (2006) 449–454.
[24] F.P. Incropera, D.P. De Witt, Fundamentals of Heat and Mass Transfer, John Wiley & Sons, 1981.
[25] E.E. Gdoutos, Fracture Mechanics Criteria and Applications, Kluwer Academic Publisher, 1990.
[26] A. Azhdari, S. Nemat-Nasser, Experimental and computational study of fracturing in an anisotropic brittle solids, Mech. Mater. 28 (1998) 247–262.